

# Testing the Flux Rope Paradigm for Coronal Mass Ejections Using a Three Spacecraft Encounter Event

Brian E. Wood<sup>1</sup>, Phillip Hess<sup>1</sup>

## ABSTRACT

We present a 3-D morphological and field reconstruction of a coronal mass ejection (CME) from 2023 November 28, which hits three spacecraft near 1 au: Wind at Earth’s L1 Lagrange point; STEREO-A with a longitudinal separation of  $6.5^\circ$  west of Earth; and Solar Orbiter (SolO) at  $10.7^\circ$  east of Earth. The reconstruction assumes a magnetic flux rope (MFR) structure for the CME. With this event, we test whether field tracings observed by a spacecraft passing near the central axis of a CME MFR (STEREO-A) can be used to successfully predict the field behavior seen by a spacecraft  $17^\circ$  away (SolO), which has a more grazing encounter with the CME. We find that the MFR model does have significant success in simultaneously reproducing the field signs and rotations seen at STEREO-A, Wind, and SolO. This provides support for the MFR paradigm for CME structure. However, the SolO measurements, which are farthest from the central axis of the MFR, show less defined MFR signatures, presumably due to a greater degree of erosion and degradation of the MFR structure far from its central axis.

*Subject headings:* Sun: coronal mass ejections (CMEs) — solar wind — interplanetary medium

## 1. Introduction

Future advancement in the understanding of coronal mass ejection (CME) structure and interplanetary evolution is likely to rely on observations that probe CME field structure in multiple locations. Traditional studies that analyze magnetic field tracings through a CME made by a single spacecraft have been invaluable in illuminating the general characteristics of field structure, guiding the development of the first models of global CME structure. In particular, the predominant magnetic flux rope (MFR) paradigm describes CMEs as tubular structures permeated by helical field, with both legs of the tube stretching back to the Sun (Lepping et al. 1990; Farrugia et al. 1995; Chen et al. 1997; Bothmer & Schwenn 1998; Vourlidas et al. 2013; Wood et al. 2017). However, proper testing of the MFR paradigm requires measurements of CME properties in multiple locations to see whether the properties of an MFR inferred locally truly apply to the global CME.

---

<sup>1</sup>Naval Research Laboratory, Space Science Division, Washington, DC 20375, USA; brian.e.wood26.civ@us.navy.mil

Past multipoint studies have mostly involved CMEs that hit spacecraft operating at different distances from the Sun, beginning with events observed by the Helios mission that probed the interplanetary medium as near as 0.3 au from the Sun (Burlaga et al. 1981), combined with observations made by spacecraft near Earth. Alignments between spacecraft operating at 1 au (e.g., Wind, ACE, STEREO) and spacecraft visiting other planets have provided other opportunities (Winslow et al. 2016; Witasse et al. 2017; Lee et al. 2018; Good et al. 2018; Lugaz et al. 2020; Palmerio et al. 2021). There are enough events of this nature that catalogs of them have been developed, allowing for a more statistical analysis of how CME properties evolve with radial expansion and propagation (Vršnak et al. 2019; Good et al. 2019; Salman et al. 2020; Scolini et al. 2022). The launches of Parker Solar Probe (PSP) in 2018 and Solar Orbiter (SolO) in 2020 provide new opportunities for multipoint CME studies (e.g., Winslow et al. 2021), with both PSP and SolO operating inside 1 au. Möstl et al. (2022) have already provided a catalog of multipoint events involving PSP and SolO, which is updated to the present year (<https://www.helioforecast.space/lineups>).

Sampling a CME’s structure at different distances from the Sun has the disadvantage of potentially confusing spatial variations in CME structure with the effects of evolutionary changes as a CME moves away from the Sun. A focus on spatial variation ideally involves multi-site sampling of a CME at the same time. An ideal opportunity for such studies has recently occurred when STEREO-A passed by Earth in 2023 August. Launched in 2006 October, the twin STEREO spacecraft have long provided stereoscopic imaging capabilities for CMEs erupting from the Sun, with one spacecraft, STEREO-A, drifting ahead of Earth in its orbit around the Sun, and one spacecraft, STEREO-B, drifting behind. With an angular drift from Earth of about  $22^\circ$  per year, the two spacecraft eventually behind the Sun in 2014-2015, when contact with the two spacecraft was lost. STEREO-A operations were successfully resumed when it emerged from behind the Sun, but such was not the case for STEREO-B. Nevertheless, STEREO-A has continued observations since then, with the spacecraft gradually drifting back toward Earth.

From 2022 July until 2024 September, STEREO-A was within  $25^\circ$  longitude of Earth, an ideal time to look for CMEs that happen to hit both STEREO-A and spacecraft operating at the Earth L1 point (e.g., Wind). The two STEREO spacecraft were also near Earth shortly after the 2006 launch date, but this was in a very inactive period for the Sun, greatly limiting the number of CMEs that hit the spacecraft while near Earth (Farrugia et al. 2011). In contrast, solar activity was quite high during the more recent passage of STEREO-A past the Sun. Nevertheless, from 2020 October until 2022 August, when STEREO-A moved from  $60^\circ$  to  $20^\circ$  from the Sun-Earth line, Lugaz et al. (2024) found only four events that hit both STEREO-A and Wind near Earth, and none of those four provided clean MFR signatures at both locations that would allow inferences of MFR orientation at the two sites. This suggests that the angular extent of CMEs in this period have generally been significantly smaller than generally assumed, with typical angular widths of only  $\sim 20^\circ - 30^\circ$ .

We here provide an analysis of an event that hit both STEREO-A and Wind at a significantly smaller angular separation of only  $6.5^\circ$ . This CME, which erupted from the Sun on 2023 Novem-

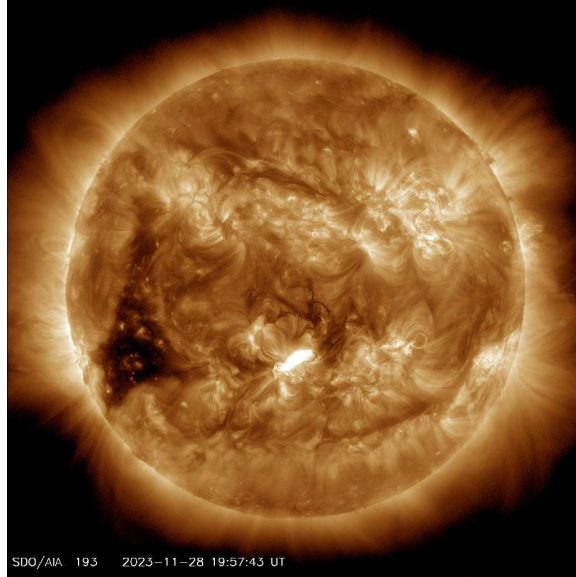


Fig. 1.— SDO/AIA 193 Å channel image showing the M9.8 flare near disk-center that accompanies the 2023 November 28 CME. Also of note is the dark coronal hole east of the flare site.

ber 28, not only hits STEREO-A and Wind but also hits a third spacecraft, SolO, which happened to be near Earth at the time in both distance and longitude. More specifically, SolO was 0.84 au from the Sun, and  $10.7^\circ$  away from Earth in longitude, in the opposite direction from STEREO-A. The event has previously been studied by Sun et al. (2024) and Chi et al. (2024). With three spacecraft tracks through the CME near 1 au, this is an ideal event for testing the MFR paradigm. We therefore provide a full 3-D reconstruction of the CME morphology based on all available white light imaging of the event; and we then assess whether a reasonable MFR field model can be inserted into the inferred MFR shape that can reproduce the field observations from all three spacecraft.

## 2. Images of the CME

At about UT 19:17:53 on 2023 November 28, an M9.8 flare began on the Sun, near disk center as viewed from Earth. Figure 1 shows an EUV image of this flare from the 193 Å channel of the Atmospheric Imaging Assembly (AIA) instrument on board the Solar Dynamics Observatory (SDO). Sun et al. (2024) provide a detailed description of the flare morphology. They decompose the surface activity into three separate erupting MFRs, though it should be noted that it is unclear how these little MFRs relate to the big CME-sized MFR that we are modeling here. The flare was accompanied by a halo CME observed by the C2 and C3 coronagraph constituents of the Large Angle Spectrometric Coronagraph (LASCO) instrument on board the Solar and Heliospheric Observatory (SOHO), which has been operating at Earth’s L1 Lagrangian point since 1996 (Brueckner et al. 1995). The CME would hit Earth on 2023 December 1, resulting in a modest  $K_p = 7$  geomagnetic storm.

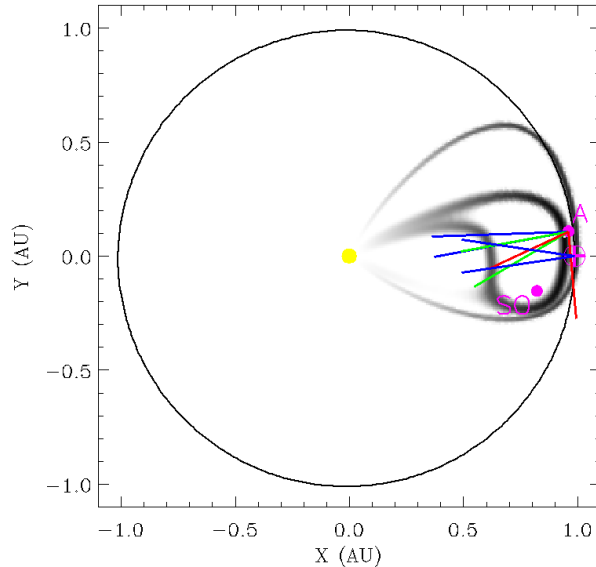


Fig. 2.— Ecliptic plane map for 2023 December 1, in an HEE coordinate system, showing the positions of STEREO-A (“A”) and Solar Orbiter (“SO”) relative to Earth. Blue lines emanating from the Earth’s location indicate the field of view of the LASCO/C3 coronagraph. Blue, green, and red lines from STEREO-A’s location indicate the fields of view of COR2-A, HI1-A, and HI2-A. The grayscale image indicates an ecliptic plane slice through the 3-D reconstruction of the 2023 November 28 CME shown in Figure 6. The lower leg of the MFR is below the ecliptic and therefore not apparent.

We here perform a full 3-D reconstruction of the morphology of this CME based on the available white light imaging of this event. This includes the aforementioned SOHO/LASCO C2 and C3 images, covering plane-of-sky distances from Sun-center of  $1.5\text{--}6 R_{\odot}$  and  $3.7\text{--}30 R_{\odot}$ , respectively. The event is also observed by the imagers on board STEREO-A. These include the COR2-A coronagraph, observing at angular distances from Sun-center of  $0.7^{\circ} - 4.2^{\circ}$  ( $2.5 - 15.6 R_{\odot}$ ), and also the HI1-A and HI2-A heliospheric imagers, viewing at  $3.9^{\circ} - 24.1^{\circ}$  and  $19^{\circ} - 89^{\circ}$ , respectively (Howard et al. 2008; Eyles et al. 2009). Figure 2 shows the location of STEREO-A in the ecliptic plane relative to Earth and SOHO, in a heliocentric Earth ecliptic (HEE) coordinate system, and also shows the fields of view of the various imagers used here. STEREO-A is only  $6.5^{\circ}$  longitude ahead of Earth at the time of the event. Also shown is an ecliptic plane slice through the 3-D reconstruction that is described in Section 4.

Figures 3-4 show a selection of the LASCO and STEREO-A images of the CME that are the basis of our 3-D reconstruction. A more thorough presentation of the imagery is provided in two movies associated with these figures. This is a halo CME from the perspectives of both SOHO/LASCO and STEREO-A. The CME is fast enough that there is a clear shock ahead of the bright ejecta, but the shock is only clearly visible to the west and north of the ejecta (see Figure 3(a)). Even though SOHO and STEREO-A are only  $6.5^{\circ}$  apart in longitude, comparison of Figure 3(b) and Figure 4(a) shows that there is still a very clear shift in the CME halo position

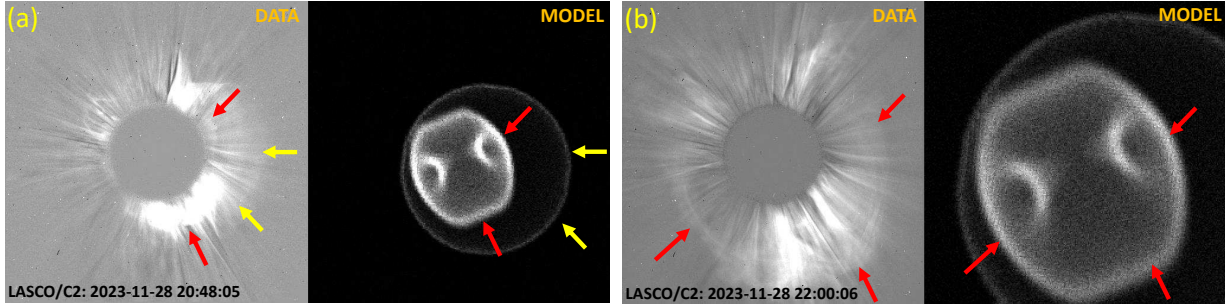


Fig. 3.— (a) The left panel is a LASCOCO/C2 image of the 2023 November 28 CME from UT 20:48:05, which can be compared with the synthetic image shown in the right panel, based on the 3-D reconstruction of the event from Figure 6. Red arrows mark the presumed leading edge of the CME ejecta, while yellow arrows mark the leading edge of a shock created by the fast CME, which is only clearly visible west and north of the ejecta. (b) Similar to (a), but for a LASCOCO/C2 image from UT 22:00:06. A movie associated with this figure provides a more comprehensive presentation of the LASCOCO data/model comparison, for both LASCOCO/C2 and LASCOCO/C3 images.

relative to the Sun. The halo is more centered on the Sun as viewed by SOHO/LASCOCO, while for COR2-A the halo center is shifted to the left of the Sun. Our determination of the CME’s central trajectory direction promises to be extremely precise due to the diagnostic power of this clear shift.

If SOHO/LASCOCO and STEREO-A were instead viewing this event from a lateral perspective, there might be little difference in the CME’s appearance in LASCOCO/C2 and COR2-A images, with a spacecraft separation of only  $6.5^\circ$ , and therefore little stereoscopic diagnostic power. But with this CME in fact directed right at SOHO/LASCOCO and STEREO-A, the situation is dramatically different. There have been many analyses trying to estimate uncertainties in CME trajectory directions from stereoscopic analysis (e.g., Verbeke et al. 2023), but the CME studied here illustrates just how difficult it is to provide uncertainty estimates for stereoscopic analysis when it can be so dependent on the exact viewing geometry.

In Section 4, we will be presenting a 3-D morphological reconstruction of the CME, assuming an MFR shape, with synthetic model images from this reconstruction shown in Figures 3-4. An attractive feature of this particular event is that we believe there is evidence for an MFR shape in the white light imaging data, particularly from STEREO-A. For a halo CME viewed from the front, the leading edge of the MFR will define the extent of the halo, while the legs of the MFR, if visible at all, should be seen as roughly circular structures on the sides of the halo, as suggested by the synthetic coronagraphic images in Figures 3-4. We believe we see this in the COR2-A and HII-A images, where we see an elliptical outline that we attribute to the top of the east leg of the MFR. Light blue ellipses are used to identify this structure in Figure 4. Structures such as this are not apparent in all halo CMEs. It is unclear what this means for the MFR paradigm, as the visibility of the MFR legs will depend on whether there is sufficient mass loaded onto the sides of

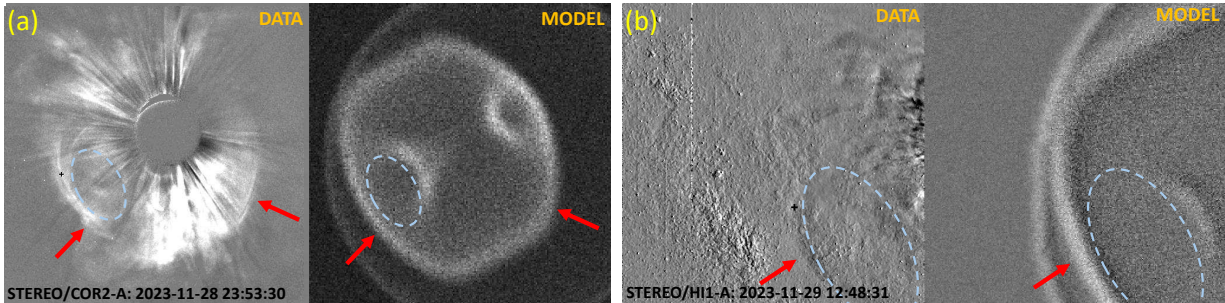


Fig. 4.— (a) The left panel is a STEREO/COR2-A coronagraphic image of the 2023 November 28 CME, which can be compared with the synthetic image shown in the right panel, based on the 3-D reconstruction of the event from Figure 6. Red arrows mark the presumed leading edge of the CME ejecta. A light blue ellipse outlines the top of the eastern leg of the MFR structure, apparent in both the real and synthetic images. (b) Similar to (a), but for a later STEREO/HI1-A image. A movie associated with this figure provides a more comprehensive presentation of the STEREO-A data/model comparison, including COR2-A, HI1-A, and HI2-A images.

the MFR legs to visibly outline them in the images. For the 2023 November 28 CME, we do see something we can interpret as the outline of an MFR leg, but in other cases the mass loading may not provide such an outline.

### 3. Kinematic Modeling

In the previous section we noted that the viewing geometry of this event promised to provide a particularly accurate determination of CME trajectory direction. In contrast, this viewing geometry is lousy for measuring CME kinematics. There is no available viewing platform that provides a lateral perspective of this event, which would allow us to properly see the CME leading edge expanding radially away from the Sun, yielding a direct indication of CME speed. Instead, the CME halo leading edges offered by SOHO/LASCO’s and STEREO-A’s frontal perspectives are indicative of lateral expansion of the CME, which we can only hope provides some constraint on the radial expansion rate.

We here use the STEREO-A images to estimate a kinematic model for the CME, where we track the more extended east side of the halo to measure leading edge elongation angle ( $\epsilon$ ) as a function of time, based on the COR2-A, HI1-A, and HI2-A images. Converting  $\epsilon$  to physical distance from Sun-center ( $r$ ) requires a geometric approximation for the shape of the CME. The two most commonly used assumptions are the “Fixed- $\phi$ ” (FP) approximation and the “Harmonic Mean” (HM) approximation. The former assumes the CME is infinitely narrow, leading to the

relation

$$r = \frac{d \sin \epsilon}{\sin(\epsilon + \phi)}, \quad (1)$$

where  $d$  is the distance from the observer to the Sun and  $\phi$  is the angle between the CME trajectory and the observer’s line of sight to the Sun (Kahler & Webb 2007; Sheeley et al. 2008). The latter approximates the CME as a sphere centered halfway between the Sun and the CME leading edge (Lugaz et al. 2009), where

$$r = \frac{2d \sin \epsilon}{1 + \sin(\epsilon + \phi)}. \quad (2)$$

The FP relation will only work for narrow CMEs where the apparent leading edge from the relevant perspective is tracking a part of the CME front that is close to the actual CME leading edge. This is very far from the case for a halo event, so the FP approximation is not a possibility here. The HM approximation should be better, but despite the success we have had in using this approximation in the past for a wide variety of events (Wood et al. 2017), we find that it fails badly here.

In the next section we will be presenting a 3-D reconstruction of the CME, and synthetic images derived from it. The kinematic model we are deriving in this section is used to describe how the 3-D model MFR CME expands with time. A successful kinematic model should result in synthetic images that have the apparent leading edge close to the observed locations, as quantified by the  $\epsilon$  values that are the starting point of the kinematic analysis. It is in this sense that the HM approximation clearly fails badly. The problem is that the HM approximation assumes a CME that is simply much too broad compared to the actual CME, which is a problem here since the apparent leading edges that we are following for our halo event are more indicative of the CME’s lateral extent than its radial distance from the Sun. We could in principle derive a kinematic model directly from the parametrized MFR shape described in the next section, but because there is no simple equation connecting  $\epsilon$  and  $r$  using the shape parameters, it would be necessary to go image by image to infer the expansion factors for the shape as a function of time that yield the correct leading edge distance. Furthermore, this tedious process would have to be repeated every time the MFR shape parameters are changed, which is impractical for the trial-and-error process of converging on a best-fit MFR shape. Thus, the use of a geometric approximation for the kinematic analysis is required.

For our kinematic model, we need a geometric approximation that assumes a narrower CME, but not as narrow as the infinitely narrow approximation represented by FP. This leads us to the “Self-Similar Expansion” (SSE) approximation championed by Davies et al. (2012). Like HM, this approximation assumes a spherical CME, but allows it to be centered anywhere between the Sun and the CME leading edge, with an extra free parameter,  $\lambda$ , indicating the angular half-width of the sphere as seen from the Sun. This leads to

$$r = d \sin \epsilon \left[ \frac{1 + \sin \lambda}{\sin(\epsilon + \phi) + \sin \lambda} \right]. \quad (3)$$

The HM equation is recovered for  $\lambda = 90^\circ$ , with lower  $\lambda$  values corresponding to narrower CMEs. Through experimentation we end up assuming  $\lambda = 15^\circ$ , with this seeming to resolve the fundamen-



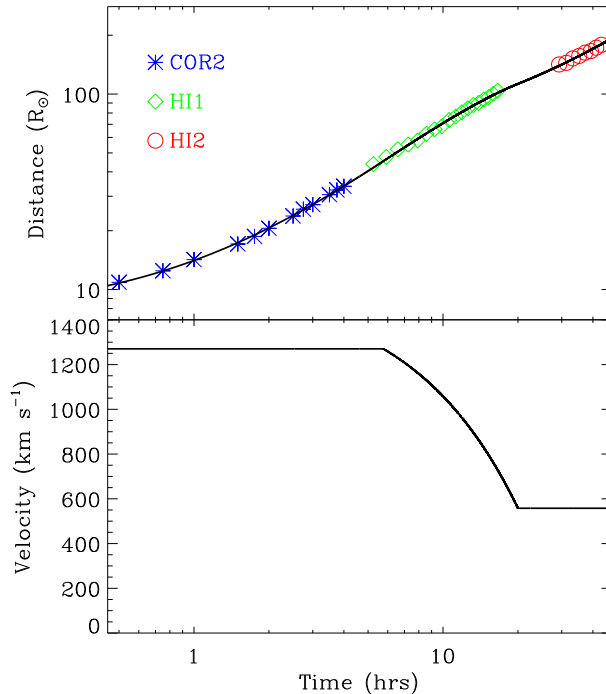


Fig. 5.— The top panel shows leading edge distance from Sun-center as a function of time for the 2023 November 28 CME, based on STEREO-A measurements from the COR2-A, HI1-A, and HI2-A imagers. The measurements are fitted with a simple three-phase kinematic model, with a phase of constant velocity, followed by one of constant acceleration, and finally another phase of constant velocity. This leads to the solid line fitted to the data points, with the bottom panel showing the inferred leading edge velocity as a function of time. The time axis is relative to the  $t = 0$  time of UT 20:53:30 on 2023 November 28.

tal difficulty with HM noted above where the synthetic images of the model MFR showed leading edges offset from the observed locations. The top panel of Figure 5 shows the resulting leading edge distances as a function of time.

For our purposes, we require a kinematic model that describes the CME’s distance from the Sun at all times, from initiation to beyond 1 au if necessary. We therefore fit the distance versus time data in Figure 5 with a simple multi-phase model, analogous to what we have done in the past (e.g., Wood et al. 2017). The three-phase model used here assumes an initial phase of constant velocity, followed by a phase of constant acceleration, and then a final phase with constant velocity. There are only five free parameters of this simple model: initial height, initial velocity, start time of phase 2, acceleration during phase 2, and end time of phase 2. The best fit is shown in the top panel of Figure 5, with the bottom panel showing the inferred velocity profile. The kinematic model suggests that the CME is at its peak speed of  $1270 \text{ km s}^{-1}$  when it enters the COR2-A field of view. It decelerates during its journey through interplanetary space, mostly while it is in the HI1-A field of view, reaching a final velocity of  $558 \text{ km s}^{-1}$ . Our peak speed estimate is in reasonably good agreement with the  $1374 \text{ km s}^{-1}$  estimate of Chi et al. (2024).



In Section 5, we will be presenting the in situ observations of this CME, from Wind, STEREO-A, and SolO. The kinematic model in Figure 5 does not do a very good job of predicting the arrival time of the CME at these spacecraft. Although the use of the SSE approximation has at least allowed a plausible kinematic model to be inferred from the  $\epsilon$  measurements, the model is still clearly imprecise.

Besides the aforementioned problem with the frontal viewing geometry, another difficulty that should be mentioned is the dubious nature of the HI2-A measurements in Figure 5. The eastern leading edge of the CME is easy to follow in COR2-A and early in HI1-A, but the leading edge fades significantly as it moves to the left side of the HI1-A field of view, where the presence of the Milky Way (see Figure 4b) makes it impossible to follow. This is the reason for the time gap between the HI1-A and HI2-A data points in Figure 5. Conclusively identifying the CME front in HI2-A beyond the Milky Way is hard. Inspection of the HI2-A movie (associated with Figure 4) shows many fairly bright fronts that are very tempting to associate with our CME. However, the timing and location of the fronts are wrong, and we believe that these fronts are background corotating interaction region (CIR) fronts associated with the high speed streams emanating from the dark coronal hole seen to the east of the flare in Figure 1. We do think we see hints of our CME front in the HI2-A movie, but the  $\epsilon$  measurements from HI2-A should be considered very uncertain, yet another reason for imprecision in the kinematic model.

For an event propagating toward the spacecraft, for the majority of the HI2-A field of view the scattering efficiency will be low and the CME can be overshadowed by brighter background features. This could also be in part why we are unable to identify the CME in any images from the SoloHI heliospheric imager (Howard et al. 2020), despite SolO being hit by the CME. SoloHI has previously been used in multiviewpoint CME studies (Hess et al. 2023), but in this case it is looking in the wrong direction, away from Sun-Earth line where most of the CME is from SolO’s perspective.

#### 4. Morphological Reconstruction

We model the 3-D morphology of the 2023 November 28 CME using a methodology utilized many times before in stereoscopic image analysis. Previous works describe how parametrized MFR shapes and shock shapes can be constructed (e.g., Wood & Howard 2009; Wood et al. 2017, 2021). Density cubes containing these structures are created, with mass placed on the surfaces to indicate the outline of the 3-D shape. No attempt is generally made to model internal MFR structure, though there have been exceptions (Wood et al. 2021). From the density cubes, synthetic images of the model CME can be made for comparison with the actual white light images of the event. Simple self-similar expansion is assumed for the CME, meaning that the shape does not change, with the kinematic model in Figure 5 defining how the scale size of the 3-D model increases with time.

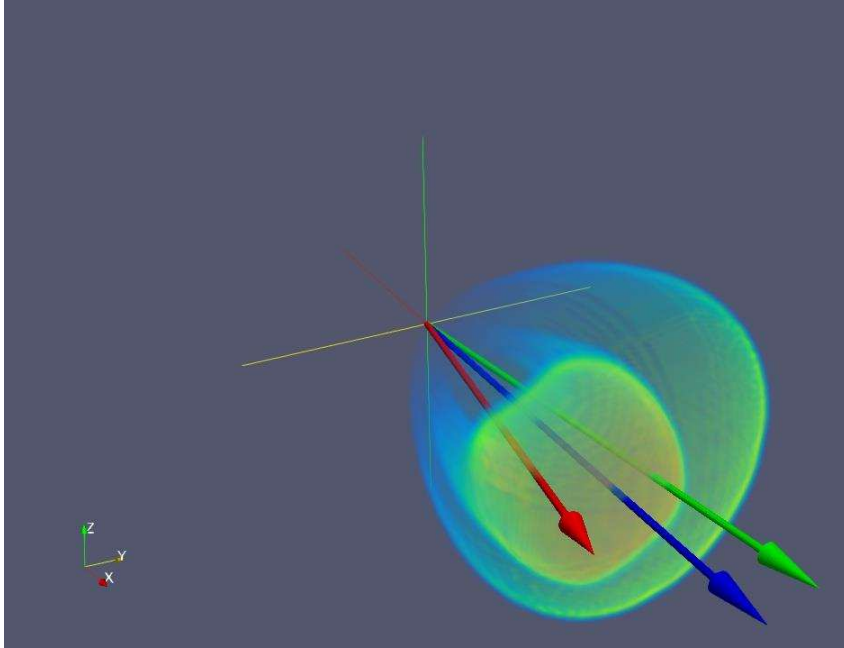


Fig. 6.— Reconstructed 3-D structure of the 2023 November 28 CME, consisting of an MFR shape and a lobular shock in front of it, shown in an HEE coordinate system. Green, blue, and red arrows indicate the directions toward STEREO-A, Wind, and SolO, respectively.

Trial and error combined with subjective judgment are used to vary the parameters of the MFR and shock shapes until a solution is found that is deemed to yield synthetic images that best match the real ones. The final morphological model is shown in Figure 6. The synthetic images associated with this model are shown in Figures 3-4, for comparison with the real ones. The two movies that accompany the figure provide a more comprehensive comparison. Because we only clearly see the shock to the west of the ejecta in the coronagraphic images, our reconstructed shock ends up asymmetric in that direction. This could be misleading, as in the HII-A data we actually do see hints that the shock may extend eastward of the ejecta as well, in a manner not reproduced by our reconstruction. Regardless, the shock is not a focal point of our study, as we are far more interested in the MFR characteristics.

Table 1 lists the best fit parameters of the 3-D reconstruction, using the variable names from Wood et al. (2017). The central trajectory is defined by  $\lambda_s$  and  $\beta_s$ , in HEE coordinates. The MFR is directed only  $\lambda_s = 2^\circ$  west of Earth in longitude and  $\beta_s = -5^\circ$  south of Earth in latitude. The  $\gamma_s$  parameter is the tilt angle of the MFR, with  $\gamma_s = 0^\circ$  corresponding to an E-W orientation parallel to the ecliptic. With a positive value of  $\gamma_s$  ( $\gamma_s = 30^\circ$ ) the west leg of the MFR is tilted upwards and the east leg downwards. This tilt is clearly indicated by the images in Figures 3(b) and 4(a), and it means that STEREO-A and Wind see a relatively direct impact of the MFR, while SolO to the east encounters the MFR much farther from its central axis. We also note that this tilt actually agrees well with the orientation of the flare in Figure 1.

Table 1: CME Morphological Parameters

Parameter	Description	MFR	Shock
$\lambda_s$ (deg)	Trajectory longitude	2	12
$\beta_s$ (deg)	Trajectory latitude	-5	-5
$\gamma_s$ (deg)	Tilt angle	30	...
$FWHM_s$ (deg)	Angular width	50.7	81.6
$\Lambda_s$	Aspect ratio	0.17	...
$\eta_s$	Ellipticity	1.6	...
$\alpha_s$	Leading Edge Shape	4	5
$x_{max}$	Leading Edge Dist.	1.0	1.05

The  $FWHM_s$  parameter is the full-width-at-half-maximum angular width of the MFR, which we find to be  $FWHM_s = 50.7^\circ$ . The aspect ratio,  $\Lambda_s = 0.17$ , indicates the minor radius of the apex of the MFR divided by the distance of the apex from the Sun. Larger values correspond to fatter MFRs. The assumed ellipticity of the MFR channel is  $\eta_s = 1.6$ , the major radius divided by the minor radius. This ellipticity is constrained by the shape of the CME halo. Reducing ellipticity and assuming a more circular channel yields a rounder outline than observed in Figures 3-4. The  $\alpha_s$  parameter defines the shape of the MFR leading edge, with high values corresponding to flatter leading edges. The MFR shape and synthetic images of it are not terribly sensitive to  $\alpha_s$  in this case, but we make our MFR flatter on top by assuming a relatively high value of  $\alpha_s = 4$ . Note that  $\eta_s$  and  $\alpha_s$  both affect time of arrival and duration predictions for spacecraft encounters, and can be modified to improve those predictions, if needed. Finally, the  $x_{max}$  parameter exists simply to indicate how advanced beyond the MFR the shock is presumed to be.

## 5. Multi-Point Field Measurements of the CME

The primary reason that this CME is worthy of special attention is that it hits multiple spacecraft near 1 au, leading to measurements of field properties at multiple locations, thereby providing an ideal opportunity to test the MFR paradigm for CME structure. In this section, we present the in situ measurements of the CME from Wind (Lepping et al. 1995; Ogilvie et al. 1995), STEREO-A (Acuña et al. 2008; Galvin et al. 2008; Luhmann et al. 2008), and SolO (Horbury et al. 2020; Owen et al. 2020). These data are obtained from publicly accessible archives supported by NASA (e.g., STEREO Science Center, SPDF/OMNI, SPDF/CDAWeb).

Figure 7 provides an overview of the solar wind properties observed by the three spacecraft between 2023 November 30 and 2023 December 5. These data are interpreted using the MFR encounter geometry implied by Figure 6, with the shaded regions in Figure 7 indicating the time periods that we associate with the MFR. With the central CME trajectory being only a little over  $5^\circ$  away from Earth, mostly to the south, it is Wind that is closest to the true apex of the MFR. STEREO-A is nearer to the west leg, and SolO to the east leg. The  $\gamma_s = 30^\circ$  tilt of the MFR centers

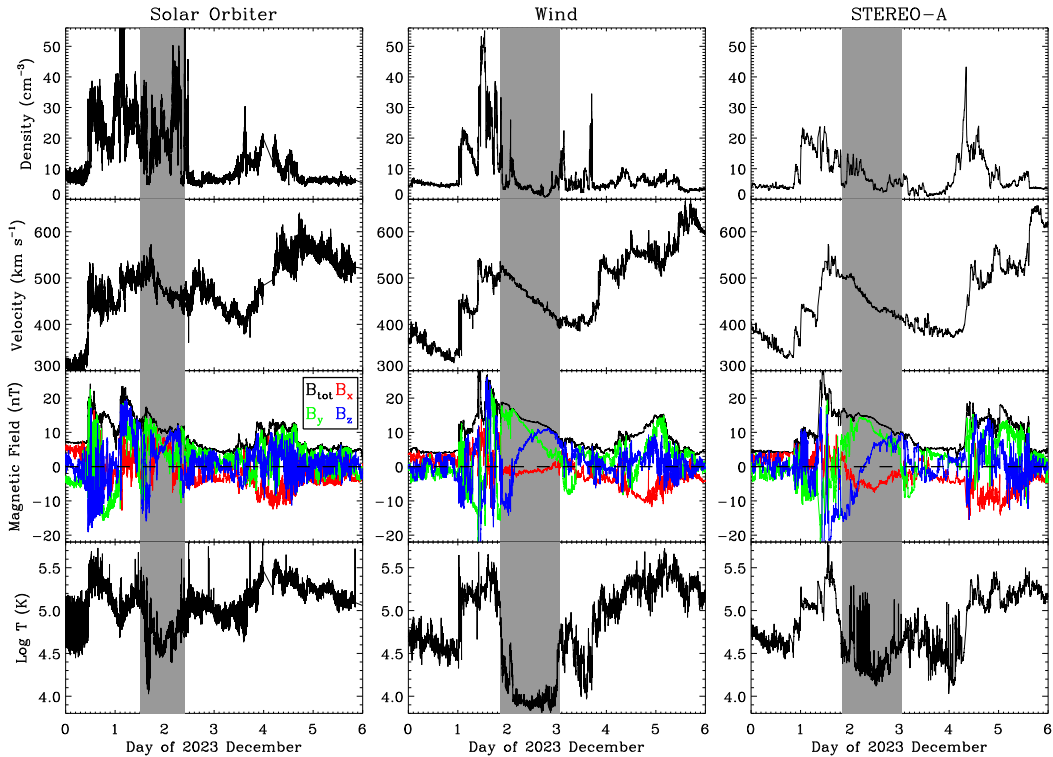


Fig. 7.— Plots of solar wind proton density, velocity, magnetic field, and temperature from 2023 November 30 through 2023 December 5, from Solar Orbiter, Wind, and STEREO-A. The magnetic field panel shows the individual field components in an RTN coordinate system, in addition to the total field. Shaded regions indicate the time periods that we associate with the MFR of the 2023 November 28 CME.

the part of the MFR that hits STEREO-A closer to the ecliptic plane, meaning that STEREO-A experiences a near direct hit by the MFR, and actually comes nearer to the central axis of the MFR than Wind does. In contrast, the MFR tilt shifts the part of the MFR that hits SolO away from the ecliptic, meaning SolO experiences more of a grazing incidence encounter with the northern edge of the MFR, significantly farther from the MFR axis than either STEREO-A or Wind. This leads to a more muddled magnetic signature than is the case for STEREO-A or Wind. (A more direct comparison of the reconstructed MFR and the in situ data will be shown in the next section.)

For Wind and STEREO-A, there is a clear phase of ordered, rotating field from late on December 1 through December 2, with low temperature and linearly decreasing velocity. These are the kinds of signatures often associated with clear in situ CME encounters. The decreasing velocity is consistent with an MFR expanding in a roughly self-similar fashion as it moves away from the Sun. The field rotations are very similar for Wind and STEREO-A, with  $B_z$  rotating from negative to positive values, and  $B_y$  with generally decreasing positive values. Even though the MFR signatures for SolO are less clear and ordered, it is important to note that the same  $B_z$  and  $B_y$  variation is still apparent, as is the decreasing velocity.

The MFR temperature signature shows interesting variation along the structure. The lowest plasma temperatures inside the MFR are seen for Wind closest to the apex. The temperatures at STEREO-A are noticeably higher, and they are higher still at SolO. The density signatures show analogous variation, with the lowest internal MFR densities seen by Wind, somewhat higher densities at STEREO-A, and much higher densities at SolO. The higher densities and temperatures at SolO are consistent with the idea that regions of the MFR far from its axis are more contaminated by incursions of plasma from the ambient solar wind through which the MFR is traveling. Such incursions may be indicative of MFR erosion, possibly due to small-scale reconnection events in the sheath region ahead of the MFR. The observations of this CME could therefore provide useful tests for models of CME MFR erosion.

Signatures of the CME’s interaction with the ambient solar wind are also apparent in the extended sheath region ahead of what we are interpreting as the MFR, which hits SolO midway through November 30 and Wind/STEREO-A at the beginning of December 1, lasting roughly a day in each case before the MFR arrival. The sheath could be predominantly quiescent solar wind heated and compressed by the CME shock. With the Sun being quite active, it could also include smaller eruptive magnetic structures swept up by the faster CME between the Sun and 1 au. Chi et al. (2024) interpret parts of the sheath as being due to two particular CMEs, which are visible in coronagraph images early on November 28, and are possibly swept up by the faster event studied here.

It is also worth noting that after the MFR, a CIR structure sweeps over the three spacecraft sequentially on December 3-4, from SolO to Wind and finally to STEREO-A. The CIR period is characterized by initial enhancements in density and field strength, and by high wind velocities and temperatures that persist past December 5. This CIR is caused by the high speed wind streams emanating from the coronal hole apparent east of the flare in Figure 1. In Section 3, we noted that the HI2-A movies show visible fronts associated with this CIR.

## 6. Field Insertion into the Model Flux Rope

In order to test the MFR paradigm, in this section we insert a physically plausible field structure into the 3-D shape inferred from white light imaging of the 2023 November 28 CME (see Figure 6), in order to see if the resulting 3-D CME field model can simultaneously reproduce the field signatures seen at all three spacecraft hit by the CME near 1 au. Our methodology for inserting a field structure into our MFR shell is the same as that in Wood et al. (2020) for a pair of CMEs from 2012 August 2 with both in situ and radio Faraday rotation constraints on field structure. The physical basis for this procedure is the MFR model of Nieves-Chinchilla et al. (2018), which is notable for allowing for MFRs with elliptical cross sections. Essentially, the Nieves-Chinchilla et al. (2018) model is used to define the 2-D field structure at the apex of our MFR, and then simplifying physical assumptions are used to extrapolate that apex field model throughout the 3-D MFR.

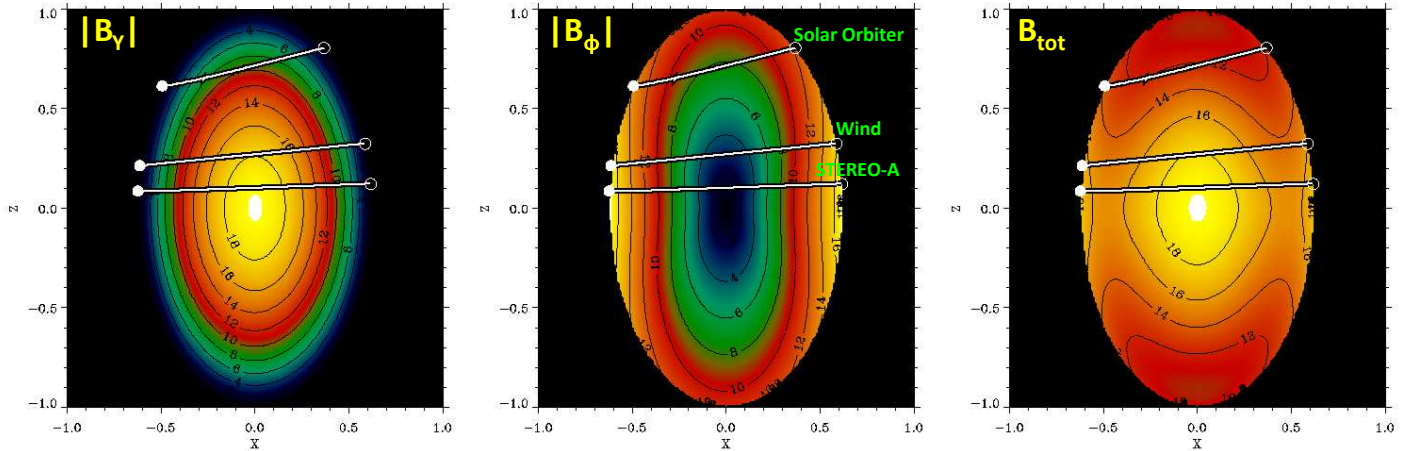


Fig. 8.— Maps of the magnetic field at the apex of the MFR for the 2023 November 28 CME, based on the model that best fits the in-situ data from STEREO-A (see Figure 9). From left to right, the maps show the axial field ( $|B_Y|$ ), the azimuthal field along the elliptical contours of the MFR channel ( $|B_\phi|$ ), and the total field ( $B_{tot}$ ). The contours indicate the field values in units of nT. The values shown correspond to the time when the leading edge of the CME reaches 1 au. The white lines indicates the paths of Solar Orbiter, Wind, and STEREO-A through the MFR channel, which move from right to left through the MFR.

With the ellipticity of the MFR having been determined observationally by imaging, a 2-D apex field map for the MFR is defined entirely by only two free parameters, the axial field at the MFR center,  $B_t$ , and the maximum azimuthal field at the surface of the MFR,  $B_p$ . We refer the reader to Nieves-Chinchilla et al. (2018) and Wood et al. (2020) for details of that computation. Figure 8 shows maps of axial field,  $B_Y$ , and azimuthal field  $B_\phi$ , based on  $B_t = -19.3$  nT and  $B_p = +17.4$  nT, best-fit values determined as described later. The axial field has the peak value of  $B_t$  at MFR center, decreasing to zero at the MFR surface. In contrast,  $B_\phi$  is zero at the axis but increases toward the MFR surface, with a maximum,  $B_p$ , at the surface along the minor axis of the ellipse. As a sign convention, we assume the negative  $B_t$  corresponds to a direction into the plane for  $B_Y$ , and a positive  $B_p$  corresponds to a right-handed MFR, meaning the  $B_\phi$  field lines follow elliptical contours in a clockwise direction in Figure 8.

The axial field is relatively easy to extrapolate from the apex to anywhere within the MFR, since flux must be conserved along the MFR, meaning that  $B_Y$  must scale as the inverse of the cross-sectional area along the MFR. There is less clarity about what is best assumed for  $B_\phi$ . Following Wood et al. (2020), we assume  $B_\phi \propto 1/a_{min}$ , where  $a_{min}$  is the local minor radius of the MFR channel. With this assumption, both  $B_Y$  and  $B_\phi$  increase into the narrower legs of the MFR, but  $B_Y$  increases more, making the field more axial in the legs than in the apex. It should be emphasized that a field structure inserted into an arbitrary 3-D MFR shape in this fashion will not be divergence free, and will only approximate a physically proper flux rope.

The MFR fields are naturally time-dependent. The reference time that we use to define the initial field model, corresponding to the apex maps in Figure 8, is when the leading edge distance from the Sun,  $R_{le}$ , of the MFR is 1 au. Because we are assuming simple self-similar expansion of the MFR with time, this implies  $B_Y$  and  $B_\phi$  both scale as  $1/R_{le}^2$ . The kinematic model in Figure 5, specifically the top panel, explicitly shows how  $R_{le}$  changes with time. With this information, we can now take an apex field map like that in Figure 8 and not only extrapolate it anywhere within the MFR, but also extrapolate it to any time during the MFR’s expansion into interplanetary space.

With the 3-D field insertion procedure now described, we can now focus on the field properties predicted by this model for the three spacecraft hit by the CME. Figure 8 provides an indication of the tracks of the spacecraft through the MFR channel, with the spacecraft moving from right to left through the channel. This depicts more explicitly the encounter geometries described in Section 4. Thanks to the  $\gamma_s = 30^\circ$  tilt of the MFR, STEREO-A near the west leg of the MFR sees a more direct hit than Wind, coming closer to the central axis, even though Wind is closer to the apex. In contrast, the  $\gamma_s = 30^\circ$  tilt shifts SolO near the east leg of the MFR away from its axis. The  $+3.8^\circ$  north latitude of SolO above the ecliptic also contributes to this shift. Incidentally, the reason the spacecraft tracks in Figure 8 show positive slopes is because of the presumed self-similar expansion of the MFR as it encounters the spacecraft.

Figure 9 shows the field components observed by the three spacecraft as they encounter the MFR. These can be compared with MFR model predictions, but first an assessment must be made about the degree to which the kinematic and morphological reconstruction described in Sections 3 and 4 successfully predict the MFR arrival times and encounter durations at the three spacecraft. We find that the arrival time predictions are very poor, but the encounter duration predictions are acceptable. In comparing model predictions with data, we have to arbitrarily shift the arrival time forward by 0.65 days. The shortcomings of the kinematic model have already been noted in Section 3. The early arrival time prediction of the model exists despite a final velocity prediction,  $558 \text{ km s}^{-1}$  (see Figure 5), that is somewhat faster than the observed peak velocity,  $\sim 520 \text{ km s}^{-1}$  (see Figure 7).

In fitting the in situ field data to find the best MFR model, we decide to fit only the STEREO-A data, which show the closest passage to the MFR axis, and we then see if the resulting MFR model can successfully reproduce the field behavior seen at Wind and SolO. We simultaneously fit all four of the field quantities shown in Figure 9 ( $B_{tot}$ ,  $B_x$ ,  $B_y$ , and  $B_z$ ). Fitting  $B_{tot}$  seems redundant, but we believe it is advantageous for the fit to include this positive-definite quantity as a constraint. As noted above, there are actually only two free parameters of this fit,  $B_t$  and  $B_p$ . The best least-squares fit to the STEREO-A data is shown in Figure 9, with  $B_t = -19.3 \text{ nT}$  and  $B_p = +17.4 \text{ nT}$ , with the apex field maps shown in Figure 8. The negative  $B_t$  value means that the left (e.g., east) leg of the MFR in Figure 6 is the positive polarity leg, and the right (e.g., west) leg is negative polarity. Incidentally, we find that a fit to the Wind data instead of STEREO-A leads to a similar quantitative result, with  $B_t = -21.9 \text{ nT}$  and  $B_p = +18.1 \text{ nT}$ . The STEREO-A MFR model is used to predict the field tracings at Wind and SolO, and these predictions are also



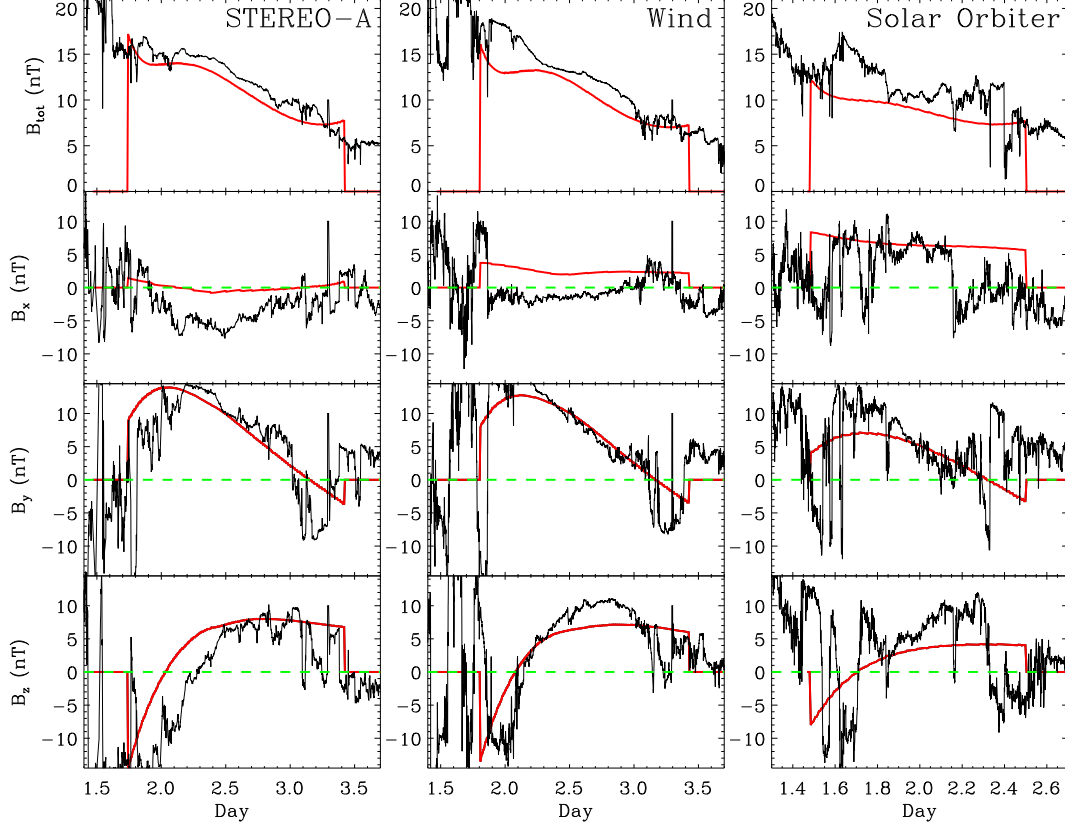


Fig. 9.— Plots of  $B_{tot}$ ,  $B_x$ ,  $B_y$ , and  $B_z$  observed by STEREO-A, Wind, and Solar Orbiter in 2023 December, showing the field variations associated with the MFR of the 2023 November 28 CME. The STEREO-A data are fitted with a field model inserted into the MFR structure shown in Figure 6. Red lines show the resulting best fit with  $B_t = -19.3$  nT and  $B_p = +17.4$  nT, shifted forward by 0.65 days. This model is then used to predict the field that Wind and Solar Orbiter should see, shown as red lines in those panels.

compared with the Wind and SolO data in Figure 9.

The fit is reasonably successful at reproducing the observed field signs and rotations, especially considering that there are only two free parameters. The STEREO-A fit predicts the Wind field measurements well, as expected given that the paths of STEREO-A and Wind through the MFR channel are similar and the observed field orientations are as well. There are still small but clear differences in field between Wind and STEREO-A despite the small  $6.5^\circ$  spacecraft separation, but field differences have been seen for even smaller separations (Regnault et al. 2024). The factor of two decrease in total field strength during the STEREO-A and Wind MFR encounters is largely due to the self-similar expansion of the MFR during the encounters. The change in  $B_z$  sign from negative to positive indicates a clockwise azimuthal  $B_\phi$  field, corresponding to the positive  $B_p$ . The  $B_x$  components observed for STEREO-A and Wind are lower than predicted by the model by about 5 nT. The simplest way to explain this is if the front of the real CME MFR is not perfectly perpendicular to the CME trajectory direction, but has a  $\sim 15^\circ$  tilt in the right direction for the

axial field,  $B_Y$ , to have a small negative  $B_x$  component.

The best test of the MFR field model comes from the SolO measurements, given that SolO is farther from STEREO-A than Wind, and encounters the MFR much farther from its central axis than either STEREO-A or Wind. In a broad sense, the model successfully predicts the general field signs and rotations observed by SolO. The  $B_y$  component is positive but decreasing, as predicted, and  $B_z$  generally changes from negative to positive, also as predicted.

However, it is  $B_x$  that is particularly worthy of note. The  $B_x$  component is mostly from the azimuthal field,  $B_\phi$ , with the x-direction pointing roughly to the right in the  $B_\phi$  panel of Figure 8. With STEREO-A and Wind passing close to the MFR axis, they are not predicted to see much field in the  $B_x$  direction, and they don't. In contrast, SolO grazes the top of the MFR where the azimuthal field is partly in the positive x-direction. Thus, SolO is predicted to see a significant positive and roughly flat  $B_x$  field profile, and this is in fact observed. This is the most impressive successful prediction of the MFR model. We conclude that a simple MFR model with an orientation inferred from imaging data is able to simultaneously explain the field tracings seen by the three spacecraft that encounter the 2023 November 28 CME to an acceptable degree, and that these data therefore provide support for the MFR paradigm.

However, the SolO field measurements within the MFR are not nearly as smooth as for STEREO-A and Wind, showing far more excursions and anomalies. We previously noted in Section 5 the higher plasma densities and temperatures seen within the MFR region by SolO. We interpret these measurements as indications of the erosion and degradation of the MFR along its periphery. The observations of this CME are particularly useful for studying this, since there are measurements of both the periphery of the MFR channel, from SolO, and measurements near the MFR axis for comparison, from Wind and STEREO-A, showing a much cleaner MFR signature.

## 7. Summary

We have presented both imaging and in situ observations of an Earth-directed CME that erupted on 2023 November 28. The CME is of particular interest for hitting three spacecraft near 1 au: Wind near Earth, STEREO-A  $6.5^\circ$  west of Earth, and SolO  $10.7^\circ$  east of Earth in longitude. Our findings can be summarized as follows:

1. We perform a full 3-D morphological and kinematic reconstruction of the event, based on imaging from SOHO/LASCO and STEREO-A. This yields an MFR shape for the CME, which is assumed to expand away from the Sun in a self-similar manner, with a peak speed of  $1270 \text{ km s}^{-1}$ , decelerating to a final speed of  $558 \text{ km s}^{-1}$ .
2. Wind and STEREO-A are inferred to sustain direct hits with the MFR, passing close to its central axis. In contrast, SolO experiences a more grazing incidence encounter along the northern edge of the MFR. The MFR signatures in the Wind and STEREO-A in situ data are

fairly clear, with smoothly rotating fields, linearly declining velocity, low temperature, and low density. In contrast, the SolO MFR signature is more confused, with higher temperatures, much higher densities, and numerous anomalies in the field measurements. The interpretation is that this is due to substantial MFR erosion and degradation on the periphery of the MFR.

3. With no lateral view of the CME, our kinematic model of the event carries large uncertainties, leading to inaccurate predictions for the CME’s arrival at Wind, STEREO-A, and SolO. We have to shift the arrival time forward by 0.65 days to agree with the in situ data.
4. For confronting the in situ data, we insert a plausible field structure into the MFR shape based on the methodology described by Wood et al. (2020) and Nieves-Chinchilla et al. (2018), which allows the field structure to be entirely defined by two parameters: the central axial field at the MFR apex,  $B_t$ , and the peak azimuthal field at the surface of the MFR at its apex,  $B_p$ . We first fit the STEREO-A in situ data, finding that  $B_t = -19.3$  nT and  $B_p = +17.4$  nT best fit these data. We then assess whether this MFR model also fits the Wind and SolO in situ data, and we find that it does so reasonably well.
5. The general agreement with the SolO data means that we have demonstrated that for this event our MFR field model can successfully be used to infer field measurements made along the periphery of the MFR in one location (e.g., SolO) based on field measurements made  $17^\circ$  degree away near the MFR axis by another spacecraft (e.g., STEREO-A). This provides support for the MFR paradigm for CME field structure, and demonstrates that despite evidence of MFR erosion and degradation on the periphery of the MFR, there is still a coherent large-scale MFR field structure defining the core of this CME.

Financial support was provided by the Office of Naval Research. We acknowledge use of NASA/GSFC’s Space Physics Data Facility’s OMNIWeb and CDAWeb services, and OMNI data. We also acknowledge the use of images from the SDO mission, courtesy of the NASA SDO and AIA science teams. The STEREO imaging data from the SECCHI instrument are produced by a consortium of NRL (US), LMSAL (US), NASA/GSFC (US), RAL (UK), UBHAM (UK), MPS (Germany), CSL (Belgium), IOTA (France), and IAS (France). In addition to funding by NASA, NRL also received support from the USAF Space Test Program and ONR. This work has also made use of data provided by the STEREO PLASTIC and IMPACT teams, available at the STEREO Science Center website, supported by NASA contracts NAS5-00132 and NAS5-00133. Solar Orbiter is a mission of international cooperation between ESA and NASA, operated by ESA. Solar Orbiter magnetometer (MAG) data was provided by Imperial College London and supported by the UK Space Agency. The Solar Orbiter Solar Wind Analyser (SWA) scientific sensors, SWA-EAS, SWA-PAS, SWA-HIS, and the SWA-DPU have been designed and created, and are operated under funding provided in numerous contracts from the UK Space Agency (UKSA), the UK Science and Technology Facilities Council (STFC), the Agenzia Spaziale Italiana (ASI), the Centre National

d’Etudes Spatiales (CNES, France), the Centre National de la Recherche Scientifique (CNRS, France), the Czech contribution to the ESA PRODEX programme, and NASA.

## REFERENCES

- Acuña, M. H., Curtis, D. W., Scheifele, J. L., et al. 2008, *Space Sci. Rev.*, 136, 203
- Bothmer, V., & Schwenn, R. 1998, *Ann. Geophys.*, 16, 1
- Brueckner, G. E., Howard, R. A., Koomen, M. J., et al. 1995, *Sol. Phys.*, 162, 357
- Burlaga, L, Sittler, E., Mariani, F., & Schwenn, R. 1981, *JGR*, 86, 6673
- Chen, J., Howard, R. A., Brueckner, G. E., et al. 1997, *ApJ*, 490, L191
- Chi, Y., Shen, C., Zhang, Z., et al. 2024, *ApJ*, 975, L25
- Davies, J. A., Harrison, R. A., Perry, C. H., et al. 2012, *ApJ*, 750, 23
- Eyles, C. J., Harrison, R. A., Davis, C. J., et al. 2009, *Sol. Phys.*, 254, 387
- Farrugia, C. J., Berdichevsky, D. B., Möstl, C., et al. 2011, *JASTP*, 73, 1254
- Farrugia, C. J., Osherovich, V. A., & Burlaga, L. F. 1995, *JGR*, 100, 12293
- Galvin, A. B., Kistler, L. M., Popecki, M. A., et al. 2008, *Space Sci. Rev.*, 136, 437
- Good, S. W., Forsyth, R. J., Eastwood, J. P., & Möstl, C. 2018, *Sol. Phys.*, 293, 52
- Good, S. W., Kilpua, E. K. J., LaMoury, A. T., et al. 2019, *JGR*, 124, 4960
- Hess, P., Colaninno, R. C., Vourlidas, A., Howard, R. A., & Stenborg, G. 2023, *A&A*, 679, A149
- Horbury, T. S., O’Brien, H., Carrasco Blazquez, I., et al. 2020, *A&A*, 642, A9
- Howard, R. A., Moses, J. D., Vourlidas, A., et al. 2008, *Space Sci. Rev.*, 136, 67
- Howard, R. A., Vourlidas, A., Colaninno, R. C., et al. 2020, *A&A*, 642, A13
- Kahler, S. W., & Webb, D. F. 2007, *JGR*, 112, A09103
- Lee, C. O., Jakosky, B. M., Luhmann, J. G., et al. 2018, *GRL*, 45, 8871
- Lepping, R. P., Acuña, M. H., Burlaga, L. F., et al. 1995, *Space Sci. Rev.*, 71, 207
- Lepping, R. P., Jones, J. A., & Burlaga, L. F. 1990, *JGR*, 95, 11957
- Lugaz, N., Vourlidas, A., & Roussev, I. I. 2009, *Ann. Geophys.*, 27, 3479

- Lugaz, N., Winslow, R. M., & Farrugia, C. J. 2020, *JGR*, 125, e27213
- Lugaz, N., Zhuang, B., Scolini, C., et al. 2024, *ApJ*, 962, 193
- Luhmann, J. G., Curtis, D. W., Schroeder, P., et al. 2008, *Space Sci. Rev.*, 136, 117
- Möstl, C., Weiss, A. J., Reiss, M. A., et al. 2022, *ApJL*, 924, L6
- Nieves-Chinchilla, T., Linton, M. G., Hidalgo, M. A., & Vourlidas, A. 2018, *ApJ*, 861, 139
- Ogilvie, K. W., Chornay, D. J., Fritzenreiter, R. J., et al. 1995, *Space Sci. Rev.*, 71, 207
- Owen, C. J., Bruno, R., Livi, S., et al. 2020, *A&A*, 642, A16
- Palmerio, E., Nieves-Chinchilla, T., Kilpua, E. K. J., et al. 2021, *JGR*, 126, e2021JA029770
- Regnault, F., Al-Haddad, N., Lugaz, N., et al. 2024, *ApJ*, 962, 190
- Salman, T. M., Winslow, R. M., & Lugaz, N. 2020, *JGR*, 125, e27084
- Scolini, C., Winslow, R. M., Lugaz, N., et al. 2022, *ApJ*, 927, 102
- Sheeley, N. R., Jr., Herbst, A. D., Palatchi, C. A., et al. 2008, *ApJ*, 675, 853
- Sun, Z., Li, T., Hou, Y., et al. 2024, *Sol. Phys.*, 299, 93
- Verbeke, C., Mays, M. L., Kay, C., et al. 2023, *AdSpR*, 72, 5243
- Vourlidas, A., Lynch, B. J., Howard, R. A., & Li, Y. 2013, *Sol. Phys.*, 284, 179
- Vršnak, B., Amerstorfer, T., Dumbović, M., et al. 2019, *ApJ*, 877, 77
- Winslow, R. M., Lugaz, N., Schwadron, N. A., et al. 2016, *JGR*, 121, 6092
- Winslow, R. M., Lugaz, N., Scolini, C., & Galvin, A. B. 2021, *ApJ*, 916, 94
- Witasse, O., Sánchez-Cano, B., Mays, M. L., et al. 2017, *JGR*, 122, 7865
- Wood, B. E., Braga, C. R., & Vourlidas, A. 2021, *ApJ*, 922, 234
- Wood, B. E., & Howard, R. A. 2009, *ApJ*, 702, 901
- Wood, B. E., Tun-Beltran, S., Kooi, J. E., Polisensky, E. J., & Nieves-Chinchilla, T. 2020, *ApJ*, 896, 99
- Wood, B. E., Wu, C. -C., Lepping, R. P., et al. 2017, *ApJS*, 229, 29